Case Studies in Thermal Engineering 25 (2021) 100885

Contents lists available at ScienceDirect

Case Studies in Thermal Engineering

journal homepage: http://www.elsevier.com/locate/csite

Thermal modelling of alternating current square waveform arc welding

Uttam Kumar Mohanty [a], Abhay Sharma [b,*], Yohei Abe [c], Takahiro Fujimoto [c], Mitsuyoshi Nakatani [c], Akikazu Kitagawa [c], Manabu Tanaka [d], Tetsuo Suga [d]

[a] Department of Mechanical and Aerospace Engineering, Indian Institute of Technology Hyderabad, Sangareddy, India
[b] KU Leuven, Faculty of Engineering Technology, Department of Materials Engineering, Campus De Nayer, Sint-Katelijne Waver, Belgium
[c] Technical Research Institute, Hitachi Zosen Corporation, Osaka, Japan
[d] Joining and Welding Research Institute, Osaka University, Japan

ARTICLE INFO

Keywords:
Welding
Heat source model
Heat transfer
Weld-pool dimension
Transient temperature
Finite element method

ABSTRACT

The instantaneous change of polarity during the welding with square waveform alternative current (AC) creates two distinct but partially overlapping weld-pools. The conventional ellipsoidal heat source model lacks the versatility to embody the overlapping weld-pools in the numerical simulation. A new overlapping double ellipsoidal heat source model is proposed to simulate the thermal behaviour of the AC square waveform welding process. The dimensions of the overlapping heat source are determined first by solving the steady-state heat conduction equation. The heat source so developed is then used in finite element analysis for the computation of the transient temperature distribution. The numerical model is validated by comparison with the experimentally measured thermal cycle. The effect of process parameters, namely welding current, electrode negative ratio, current frequency, on the thermal behaviour and weld-pool geometry is analyzed. The interplay between the process parameters and the thermal cycle due to AC square waveform are the significant findings of the present work, e.g., increase in frequency stabilizes the arc on the cost of lowering the peak temperature. The computationally affordable welding heat transfer models, such as the present investigation, pave the way to resolve shop-floor significant issues such as residual stress and distortion.

1. Introduction

Submerged arc welding (SAW) process, because of the high deposition rates, is the most common arc welding process used in the pressure vessel and pipeline industry. The heat generation in the SAW occurs due to the arc between the consumable wire electrode and the workpiece, which is submerged beneath a layer of fusible granular flux. Conventionally, direct current in positive or negative polarities is used with SAW. The alternating current (AC) is used with one of the electrodes in multi-wire SAW. The use of sine or triangular AC waveform in single-wire SAW risks the arc extinction at the time of polarity reversal. In recent years, the square AC is successfully used with single-wire SAW. The AC square waveform power source provides uniform deposition and penetration because of the instantaneous polarity reversal without extinguishing the arc [1]. The AC power also minimizes the arc blow. The shape of AC square waveform weld-pool is considerably different from the regular semi-ellipsoidal weld-pool obtained with direct current (DC), as

* Corresponding author.
E-mail address: abhay.sharma@kuleuven.be (A. Sharma).

https://doi.org/10.1016/j.csite.2021.100885
Received 26 September 2020; Received in revised form 23 January 2021; Accepted 9 February 2021
Available online 12 February 2021

shown in Fig. 1. The instantaneous polarity reversal in the square AC produces two partially overlapping but distinct weld-pools. The final weld cross-section shape depends on the proportion of time in a cycle for which the negative (and positive for the remaining) currents remain active; vis-a-vis electrode negative (EN ratio), which is the proportion of the time in a cycle the electrode remains negative.

The weld-pool shape change directly impacts the weld properties; for example, the hardness distribution in the weld cross-section [2]. The thermal cycle produced by the moving heat source (i.e., welding arc) with a high heat generation rate is the cause of the metallurgical changes in the weld. Understanding the physical phenomena of the arc is complex because of the complicated mechanism that occurs in the arc column, at the arc-electrode interface, and in the molten and solid region of the workpiece. However, the weld thermal cycles in the body of the workpiece can be simulated by solving the transient heat conduction equation given as follows:

$$\nabla.(K\nabla T) + Q_g = \rho c_p \frac{DT}{Dt} = \frac{DH}{Dt} \tag{1}$$

K is thermal conductivity, T is temperature, ρ is density, C_p is specific heat, t is time, and H is enthalpy. The energy from the arc is represented by a distributive heat source (Q_g). Historically, different types of heat sources, such as the point, line, surface, and the volumetric heat sources have been used in numerical simulation of the fusion welding processes. One of the most versatile heat sources is given by Goldak et al. [3]. The Goldak's heat source considers the heat source being double ellipsoidal in shape. The rear and front halves of the heat source are quadrants of two ellipsoids with different lengths in the welding direction (x-axis), as shown in Fig. 2.

The arc energy is considered distributed in Gaussian fashion. The power density in each quadrant is given as follows:

In the front quadrant

$$Q_g(x,y,z) = \frac{6\sqrt{3} f_f Q_p}{ab_f c\,\pi\sqrt{\pi}}\, e^{-3(x-vt)^2/b_f^2} e^{-3(y)^2/a^2} e^{-3z^2/c^2} \tag{2}$$

In the rear quadrant

$$Q_g(x,y,z) = \frac{6\sqrt{3} f_r Q_p}{ab_r c\,\pi\sqrt{\pi}}\, e^{-3(x-vt)^2/b_r^2} e^{-3(y)^2/a^2} e^{-3z^2/c^2} \tag{3}$$

where, Q_p is the arc heat, a, b_f, b_r, and c are the dimensions of the ellipsoid, as shown in Fig. 2. f_f and f_r are the fractions of heat supplied to the front and rear of the arc.

In the past decade, the Goldak's model has been modified and adapted for different processes, namely, plasma arc welding [4], twin-wire welding [5], pulsed arc hybrid welding [6], laser–arc hybrid welding [7], micro electron beam welding [8], TIG-MIG hybrid welding [9], and cold metal transfer welding [10]. The approach to determine the heat source parameters (*a, b, c* in Fig. 2) is also modified from the predetermined values in the Goldak's model to more realistic approaches, for example, use of static heat transfer analysis [11], a determination based on actual bead shape [12], and application of partial least square method [13]. Besides, modifications in Goldak's model are reported for different purposes; for example, reducing the number of parameters [14], welding of narrow-groove welds [15], and effect of electrode tilt [16].

The effects of the square waveform on weld bead geometry [17] and the chemical composition of weld bead [18] are known over a decade. In the recent times, several new thermo-mechanical-metallurgical phenomena associated with the square waveform welding have emerged vis-a-vis ability to weld at higher velocity without compromising the weld penetration [19], the effect on the grain size and width of the partially melted zone [20], arc stability [21], and improved melting efficiency [22]. A better understanding of the phenomenon, as mentioned above, necessities the capability of accurate thermal simulation, which in turn requires dedicated efforts

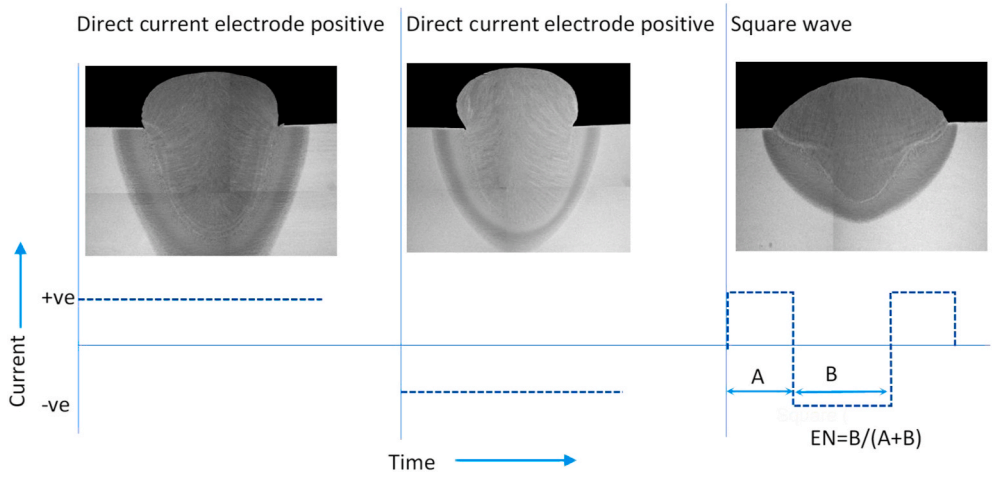

Fig. 1. Weld-pool shape change with polarity.

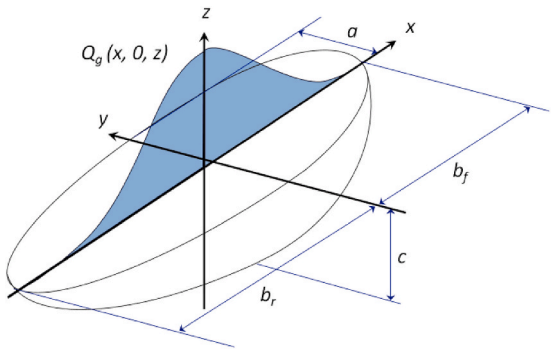

Fig. 2. Goldak's double ellipsoidal heat source.

towards developing a heat source model. The available literature does not reveal the heat transfer analysis of the AC square waveform welds produced under different process conditions. This investigation's main objective is to develop a heat source model that can further be used in finite element analysis for the AC square waveform process. This work's specific investigation is to determine the optimum parameters of heat sources for a candidate material (2.25Cr-1 Mo heat resistant steel) for predicting peak temperature at different locations in the workpiece. In what follows, the experimental work followed by the development of the heat source model is given. The model is then validated, and the effect of the various process conditions on the thermal cycle is discussed.

2. Experimentation

A rectangular 2.25 Cr-1 Mo heat resistant steel plate of 20 mm thickness was used as the workpiece material. US-521S wire of 4 mm diameter was used as the electrode material. The combination of wire and flux materials was chosen based on the AWS classification AWS A5.23 F9P2-EG-B-3 for AC power source. PF-200 bonded flux with mesh size 10 x 48 was the flux material. The dimension of the workpiece was 300 mm X 80 mm X 20 mm, and the length of the weld run was 200 mm. The heating and cooling behavior of AC square SAW affects the temperature profile in the different weld zone like weld metal zone (WM), heat affected zone (HAZ) and base metal (BM) zone. The position of the thermocouple for temperature measurement was obtained by measuring the width (W), penetration (P), heat affected zone (HAZ) width and depth from the weld macrograph in the trial experiment. The thermocouples' position, on the surface (W_1 and W_2) and inside the workpiece at the longitudinal center plane (D_1), are shown in Fig. 3. The numbers inscribed in the circles in Fig. 3 represent thermocouples' position in width and depth direction, i.e., number '1' represents the location in the depth direction and numbers '2 and 3' represent the location in the width direction, as specified in Table 3.

R-type (Pt-Pt and 13% Rh) thermocouple wire was used at the locations nearer to the WM zone in both width and depth direction (W_2 and D_1, respectively), and K-type of thermocouple wire was used for the remaining locations. The bead-on-plate welding experiments were conducted to identify the heat source parameters and subsequent validation, using different welding conditions, as shown in Table 1. The welding speed for all the experiments was set at 30 cm/min. The location of the thermocouples at (W_1, W_2, and D_1) was not similar for different welds. The locations were independently chosen for each weld such that the tip remains in the HAZ. The thermal cycles of different welding conditions are shown in Fig. 4. The corresponding locations of the thermocouples are given in Table 1.

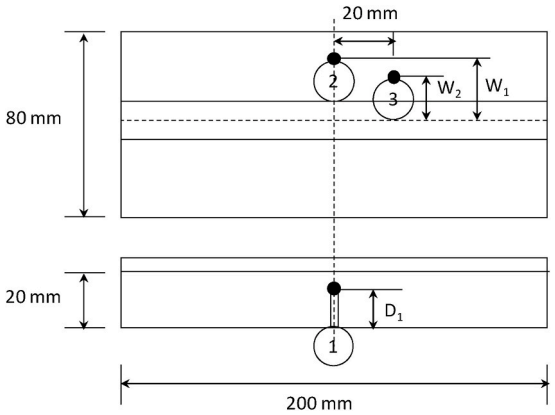

Fig. 3. Schematic diagram showing the location of the thermocouple.

Table 1
Thermal cycle measurement conditions and locations.

Exp. No	Process conditions			Thermocouple location (x, y, z)			Peak Temperature (°C)		
	F (Hz)	EN	I (A)	D_1	W_1	W_2	D_1	W_1	W_2
1	60	0.5	500	100, 0, 5.6	100, 12.93, 1	120, 13.5, 1	743.3	522	436.4
2	60	0.5	600	100, 0, 6.96	100, 14.72,1	120, 15.34,1	706.3	884.9	807
3	60	0.75	500	100, 0, 6.0	100, 12.37, 1	120, 13, 1	660.7	594.6	478.8
4	20	0.5	500	100, 0, 5.8	100, 13.5, 1	120, 14.1, 1	827.8	998.3	861

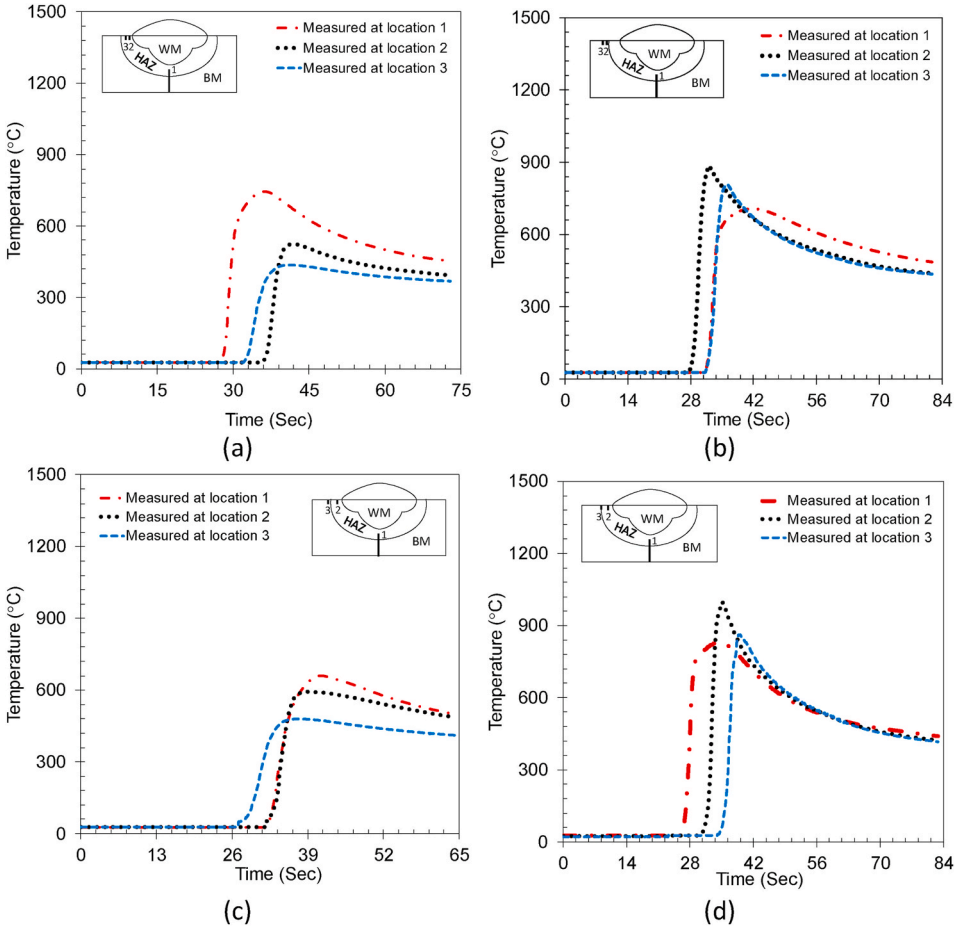

Fig. 4. Thermal cycle at different points at (a) I= 500 A, EN ratio=0.5, F=60 Hz, (b) I= 600 A, EN ratio=0.5, F=60 Hz, (*c*) I= 500 A, EN ratio=0.75, F=60 Hz and (d) I= 500 A, EN ratio=0.5, F=20 Hz.

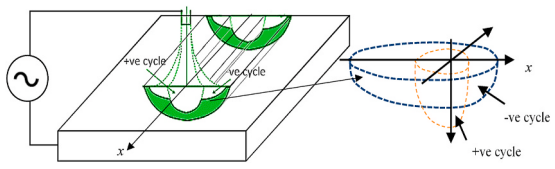

Fig. 5. Overlapping heat sources for AC square welding.

3. Mathematical formulation

3.1. Heat source model for AC square arc welding

The shape of the penetration profile inspires the shape of the heat source. The double ellipsoidal heat source, because of its generalization capabilities, is the most used heat sources for welding simulation. The double ellipsoidal heat source is characterized by the dimensions in lateral, longitudinal (i.e., front, and rear), and depth directions, a, b_f, b_r, and c, respectively. The cross-section of the AC square waveform weld is a composite profile of two individual penetrations because of polarity reversal (Fig. 1). The + ve cycle produces a deep and narrow weld-pool. The -ve cycle, on the other hand, spreads the arc that leads to a shallow and wider weld-pool. The + ve and -ve cycles have a time lag of ($1/2f$) that corresponds to a spatial difference of $v/2f$. The preliminary investigation confirmed that the spatial difference and the time lag between the two cycles are too small to impact the thermal cycle. Therefore, two overlapping heat sources with the same origin are considered, as shown in Fig. 5.

In the moving coordinate $\xi = x - vt$, where v is the welding speed, and t is the time elapsed after the arc initiation, the power density of both heat sources can be expressed as follows:

Power density for the -ve cycle heat source:

$$\text{if } \xi > 0 \quad Q_{g\_w}(x,y,z) = \frac{6\sqrt{3} f_f Q_p \phi}{a b_f c \, \pi\sqrt{\pi}} \, e^{-3(x-vt)^2/b_f^2} e^{-3y^2/a^2} e^{-3z^2/c^2} \tag{4}$$

$$\text{else if } \xi < 0 \quad Q_{g\_w}(x,y,z) = \frac{6\sqrt{3} f_r Q_p \phi}{a b_r c \, \pi\sqrt{\pi}} \, e^{-3(x-vt)^2/b_r^2} e^{-3y^2/a^2} e^{-3z^2/c^2} \tag{5}$$

$$\text{else if } \xi < 0 \quad Q_{g\_w}(x,y,z) = \frac{6\sqrt{3} Q_p \phi}{a c \, \pi\sqrt{\pi}} \left(\frac{f_f}{b_f} + \frac{f_r}{b_r}\right) e^{-3y^2/a^2} e^{-3z^2/c^2} \tag{6}$$

where, Q_{g_w} is the power density of the -ve cycle heat source and Q_p denotes the arc heat. f_f and f_r are the fractions of heat supplied to the front and rear of the arc, whose values are taken as 0.6 and 1.4, respectively, as recommended in the open literature [3]. ϕ is the flux compensation factor, which signifies the amount of heat available for melting of the plate, excluding the heat used in melting the flux [11].

Power density for the +ve cycle heat source:

$$\text{if } \xi > 0 \quad Q_{g\_p}(x,y,z) = \frac{6\sqrt{3} f_f Q_p \phi}{a b_{f1} c \, \pi\sqrt{\pi}} \, e^{-3(x-vt)^2/b_{f1}^2} e^{-3y^2/a_1^2} e^{-3z^2/c_1^2} \tag{7}$$

$$\text{else if } \xi < 0 \quad Q_{g\_p}(x,y,z) = \frac{6\sqrt{3} f_r Q_p \phi}{a b_{r1} c \, \pi\sqrt{\pi}} \, e^{-3(x-vt)^2/b_{r1}^2} e^{-3y^2/a_1^2} e^{-3z^2/c_1^2} \tag{8}$$

$$\text{else if } \xi = 0 \quad Q_{g\_p}(x,y,z) = \frac{6\sqrt{3} Q_p \phi}{a_1 c_1 \, \pi\sqrt{\pi}} \left(\frac{f_f}{b_{f1}} + \frac{f_r}{b_{r1}}\right) e^{-3y^2/a_1^2} e^{-3z^2/c_1^2} \tag{9}$$

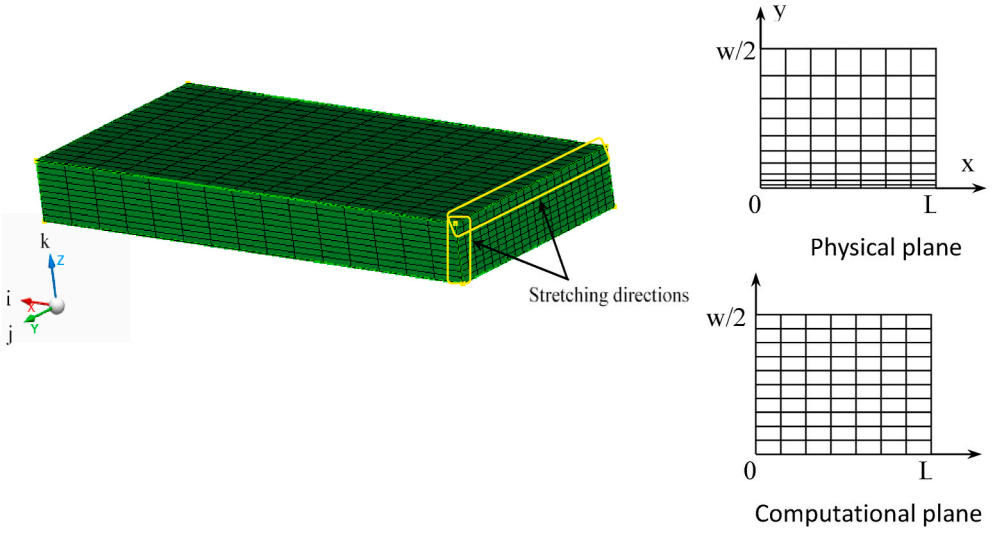

Fig. 6. Stretching transformation.

where, Q_{g_p} is the power density of the +ve cycle heat source and a_1, b_{f1}, b_{r1}, and c_1 are the dimensions of the double ellipsoidal heat source in lateral, longitudinal (i.e., front, and rear), and depth directions for the +ve cycle heat source, respectively.

The total power density can be given as

$$Q_g(x,y,z) = Q_{g\_p}(x,y,z) + Q_{g\_w}(x,y,z) \tag{10}$$

The expression for arc heat is given as follows:
For the -ve cycle heat source:

$$Q_p = \eta VI\, E \tag{11}$$

For the +ve cycle heat source:

$$Q_p = (1-E)\eta VI \tag{12}$$

where E is the EN ratio, η is the arc efficiency, which is considered as 0.95, V is the voltage, and I is the welding current.

3.2. Estimation of dimensions of heat source

The heat source dimensions are obtained from the method suggested by Sharma et al. [11] wherein the peak temperature is numerically obtained by solving the heat transfer equation in a steady state. The finite difference method is used to obtain the peak temperature. The dimensions of heat source are varied, and the set that gives the most accurate prediction of peak temperatures for several points (W_1, W_2, and D_1) is considered the heat source dimensions. The heat conduction equation (Eq. (1)) is solved for cuboid geometry, as shown in Fig. 6. The discretization of the geometry leads to a different node in x, y, and z directions, which are designated as i, j, k, respectively. The nodes in the moving heat source direction (x) are equally spaced. The mesh in the lateral and depth directions are finer in the vicinity of the weld-pool but grows towards the edge and the bottom.

The stretching transformation is used to obtain the mesh in the width direction and depth direction given in Eqs. (13) and (14), respectively.

$$y = (w/2)\left[\frac{(\beta_1+1)-(\beta_1-1)B^{1-\chi}}{1+B^{1-\chi}}\right] \tag{13}$$

where w is the bead width, β_1, and B are the constants. The value B and χ are calculated as $B = \frac{\beta_1+1}{\beta_1-1}$ and. $\chi = \frac{j}{j^{max}}$

In this expression, j^{max} represents the maximum number of nodes in the width direction. Hence, the expression $1-\chi$ becomes $\frac{j^{max}-j}{j^{max}}$.

The stretching transformation along depth direction (z) can be expressed as

$$z = d\left[\frac{(\beta_2+1)-(\beta_2-1)B^{1-\chi}}{1+B^{1-\chi}}\right] \tag{14}$$

The thermal conductivity at the interface region is calculated using the following expression.

$$K(T_1,T_2) = \frac{2}{\left(\frac{1}{K(T_1)}+\frac{1}{K(T_2)}\right)} \tag{15}$$

where $K(T_1,T_2)$ is the thermal conductivity at the interface of control volumes. The semi-discretized form of Eq. (1) with central differencing is used to find the peak temperature. At the instance of the peak temperature, the rate of change of temperature so as the enthalpy is zero, i.e., $\dot{H}_{i,j,k}$=0, leads to the equation for the peak temperature (T_p) at a given node (i, j, k).

The optimal heat source dimensions are obtained by solving the heat conduction equation through an in-house code in Matlab 2018. The values of b_f, b_r, c, b_{f1}, b_{r1}, and c_1 are obtained by minimizing error in predicting the peak temperatures of three points for each sample. The domain search method is used wherein the feasible ranges of the heat source parameters are searched by incre-

Table 2
Optimum dimensions of the heat source.

Effect	Process Condition			-ve cycle heat source dimensions				+ve cycle heat source dimensions				Flux compensation factor	Mean absolute % Error
	F (Hz)	EN	I (A)	b_f	b_r	a	c	b_{f1}	b_{r1}	a_1	c_1	ϕ	
Frequency	20	0.5	500	15.26	19.31	25.92	1.21	9	10.16	14.89	3.41	0.98	8.03
	60	0.5	500	20.41	22.94	22.00	0.90	13.96	15.78	9.83	3.30	0.76	6.81
Current	60	0.5	500	20.41	22.94	22.00	0.90	13.96	15.78	9.83	3.30	0.76	6.81
	60	0.5	600	23.20	26.14	27.50	1.21	20.87	25.05	16.00	3.82	0.95	8.77
EN ratio	60	0.5	500	20.41	22.94	22.00	0.90	13.96	15.78	9.83	3.30	0.76	6.81
	60	0.75	500	18.08	20.34	12.43	0.64	17.80	19.85	11.03	3.38	0.78	18.18

mentally changing the parameters' values and mean absolute % error in peak temperatures of the three points is recorded. The optimum dimensions obtained through the domain search and the error in predicting the peak temperatures are given in Table 2. It is quite evident that the predicted peak temperatures are in good agreement with the experimental peak temperatures for different welding conditions, except for the 0.75 EN ratio. The higher % error is because of the low peak temperatures obtained from this condition. The same absolute error results in higher % error because of the smaller reference value.

The change in the heat source dimension in Table 2 is the manifestation of the variation in heat transfer due to change in process parameters. For example, the arcing and droplet transfer rate increase with an increase in the frequency. Concurrently, around 60 Hz, arc cone shape starts becoming narrow because of lack of time to expand. As a result, the weld bead's size and the heat transfer phenomenon are also affected. The EN ratio represents the fraction of cycle time for which the electrode polarity is negative. It is well known that the positive electrode in consumable arc welding increases the penetration (melting of the workpiece) because the droplet emerging form the positive electrode has higher temperatures and thus, they impinge forcefully to the weld-pool [23]. With the same reason, the negative electrode increases the melting rate on the cost of plate melting. The proportion of plate electrode melting and the weld-pool size change with a change in the EN ratio. In Table 2, when the frequency of 500A welding current increases from 20hz to 60hz, the flux compensation factor decreases from 0.98 to 0.76. The flux compensation factor signifies the reduction in heat available for the melting of the plate because of the consumption of heat in melting the submerged arc flux. Higher frequency agitates the molten flux cavity and increases the flux melting, which eventually reduces the flux compensation factor.

3.3. Transient temperature analysis

In this section, a three-dimensional transient heat transfer model is developed to analyze the AC square SAW's temperature distribution using Simufact software. The finite element discretized workpiece, filler, bearing, and clamping material are shown in Fig. 7. The number of nodes in length, width, and penetration directions are taken as 15, 80, and 40 by 2.5D meshing option available in MSC Apex software for the workpiece material to achieve the coarse meshing and fine meshing. As the heat-spread in a moving coordinate system is quasi-static in the welding direction, the analysis is made with 2.5 D meshing. The grid size in the welding direction is larger than the other two directions. The grid size in welding, width, and depth directions are 20 mm, 1 mm and 0.5 mm, respectively. The clamp is considered as the cylindrical geometry with length 10 mm and a diameter of 16 mm. The bearing materials are 450 mm, 120 mm, and 10 mm in length, width, and depth directions, respectively.

The thermal properties (i.e., specific heat, and thermal conductivity) of both workpiece and electrode material, except density, are considered temperature-dependent, as shown in Fig. 8. The arc efficiency that accounts for the heat consumed to melt flux, electrode, and workpiece material after heat loss due to conduction, convection, and radiation, is taken as 0.95. The ambient temperature of the plate and workpiece material is considered as 27 °C. The density, latent heat of fusion, and melting point temperature are considered 7750 kg/mm^3, 232170 J/kg, and 1511.88 °C, respectively.

Two types of heat loss take place due to convection. The first type is due to the heat loss from the workpiece to the surroundings, and the second type is due to the heat loss from the contacting surface of the workpiece. The mathematical representation of convective heat loss and contact heat loss per unit area is given as follows.

$$q_c = h(T - T_0) \tag{18}$$

$$q_b = a(T_1 - T_2) \tag{19}$$

where h and a are the convective heat transfer coefficient and contact heat transfer coefficient whose values are taken as 20 W/m^2 °C and 500 W/m^2°C, respectively.

The radiation boundary condition can be expressed as the function of emissivity:

$$q_r = \varepsilon\sigma\left(T^4 - T_0^4\right) \tag{20}$$

where the value of emissivity (ε) is considered as 0.6 and Stafen Boltzmann constant (σ) is $5.67 \times 10^{-8}\ W/m^2K^4$. Four clamps are used to constrain the motion of the workpiece. The torsional stiffness and rotational stiffness for each clamping element are 1000 N/m and 100 Nm/rad, respectively.

Table 3
Comparison of weld-pool attributes and peak temperature.

Exp. No.	Width (mm)		Penetration (mm)		Peak temperature (° C)					
	Measured	Predicted	Measured	Predicted	Measured			Predicted		
					D_1	W_1	W_2	D_1	W_1	W_2
1	24.15	23.5	4.19	4.43	743.3	522	436.4	870.55	601.07	557.88
2	26.4	25.64	5.88	6.11	706.3	884.9	807	828.03	921.24	869.37
3	22.6	22.06	4.2	4.45	660.7	594.6	478.8	845.84	617.47	580.65
4	24.92	25.8	4.54	4.9	827.8	998.3	861	860.85	1097.22	925.05

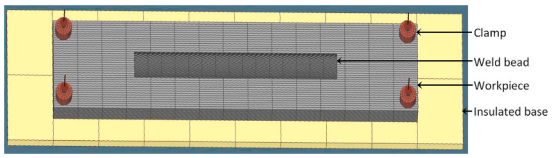

Fig. 7. Finite element discretization of the geometry of the workpiece.

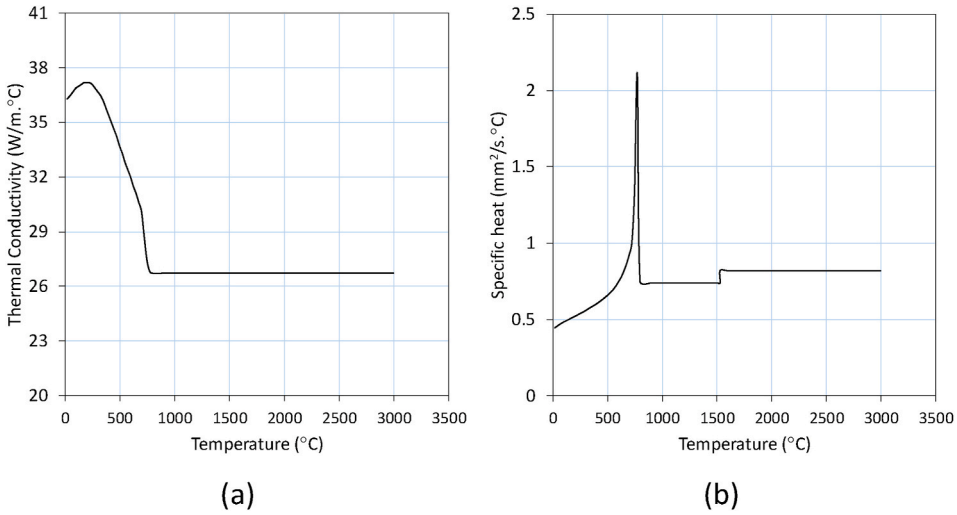

Fig. 8. Temperature-dependent (a) thermal conductivity (b) specific heat.

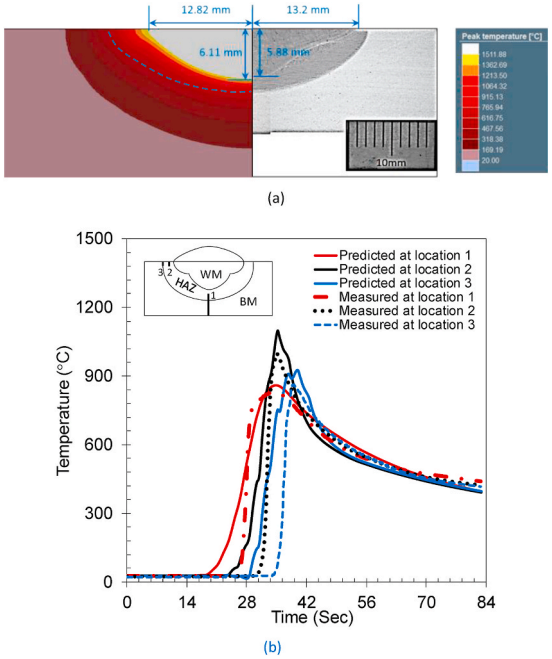

Fig. 9. Comparison between measured and simulated weld-pool at I=600 A, F=60 Hz, EN ratio= 0.5, s=30 cm/min.

4. Results and discussion

4.1. Validation of the developed model

The double ellipsoidal heat source dimensions can predict the dimension of the weld-pool. The deviation between the measured and predicted weld-pool dimensions does not exceed by 1 mm, as shown in Table 3. In addition to that, the percentage prediction error for both width and depth are also not exceeding 10%.

The predicted peak temperatures are also in agreement with the actual (measured) peak temperatures. The general agreement on weld penetration and the thermal cycle is shown in Fig. 9a and 9b, respectively. The heat source parameters are genuine representative of the heat source as the thermal cycles at the surface (W_1 and W_2) and the inner (D_1) locations are predicted with reasonably good accuracy, as shown in Fig. 9b. Fig. 9a shows the comparison between the simulated and actual weld-pool shape. The actual weld shape is in good agreement with the simulated weld-pool shape. The shape of the heat-affected zone resembles with the predicted isotherms. The simulated weld profile does not fully capture the convex shape weld metal profile. In the thermal simulation of welds, these effects, up to some extent, are addressed by considering fine meshing pattern in the weld region [24]. However, the convex shape is primarily because of the fluid flow effects. Fluid flow inside the weld-pool is related to the surface tension effect, which impacts the temperature field and changes the weld-pool's morphological appearance [25]. The action of surface tension force during the fluid flow causes two effects – surface tension generates a normal on to the free surface of the fluid related to the surface's curvature. It generates an additional tangential force through a temperature gradient on the free surface.

4.2. The relation between process conditions and the dimensions of heat source

The relation between optimized heat source dimensions and process condition are shown in Fig. 10. The expansion of the weld-pool in front and rear direction (b_f and b_r) increases with an increase in the frequency (Fig. 10). This increment is observed for + ve and -ve cycles. The increment is at the cost of a reduction in the weld width (a). The depth direction dimension does not change with change in the frequency. The spreading of the centre core of the arc is restricted because of the frequent polarity reversal at higher frequencies. The lower frequency allows + ve and -ve cycles to act for a longer duration, which is a kind of anti-phasing (time lagging) in the twin-wire welding system that influences the heat transfer pattern and changes the weld microstructure [26].

At higher frequency, the current direction changes more frequently. The arc deflects along the longitudinal direction; in the welding direction and opposite the welding direction, while the torch moves from starting to the endpoint, as observed earlier [27]. The reversal of current breaks the sheath of charged particles at the anode and cathode surfaces, which improves the stability of the arc at higher frequencies, as observed in Ref. [28]. The reversal also agitates the weld-pool and thereby reduces the weld porosity at higher frequency [29]. Higher frequency accelerates the influence of the arc deflection. A quick reversal of the current direction at higher frequency keeps the peak temperature low (20 and 60 Hz, Table 1), creating a more considerable difference between the arc and the workpiece temperature. The combined effect of deflection of the arc and the temperature difference helps spread arc in the longitudinal direction.

Interestingly, despite the difference in duration for + ve and -ve cycles at EN =0.75, both the heat sources are equally spread in the width and longitudinal direction. On the other hand, EN=0.5, i.e., equal active time for + ve and -ve cycles results in a difference in the size of heat sources in width and longitudinal direction. In a way, the square waveform acts as a combination of two heat sources that are different in time and space. Such differences impact the arc stability in the processes where multiple heat sources are used [30]. Understanding the arc stability and EN ratio relationship requires separation of current and voltage signals for + ve and-ve cycles that merits further investigation.

4.3. Parametric effects on thermal cycle

The thermal cycle of the AC square waveform welds is influenced by the heat input (welding current), current frequency, and the EN ratio, as shown in Fig. 11. The increase in the welding heat causes the rise in peak temperature because of the current increase (Fig. 11a). The cooling rate at 600 A is around 10.7 °C/sec. An increase in frequency causes a dip in the peak temperature (Fig. 11b). The change in frequency does not change in the heat input, but changes the heat spread pattern, as discussed earlier. Due to the increase in heat spreading, the peak temperature slightly reduces at a higher frequency. The cooling rate does not alter with a change in the frequency. The EN ratio increase from 0.5 to 0.75 causes a small dip in the peak temperature and the cooling rate (Fig. 11C). The increase in the melting rate and the shallow weld-pool without a change in total heat input causes the dip in the peak temperature and the cooling rates.

The modelling of the welding process based on pure heat transfer analysis is vital to understand the residual stress and distortion phenomenon. The fluid dynamics-based models provide details of the weld-pool; however, they are too computationally prohibitive to implement for the complex welding processes or applications like additive manufacturing. Consequently, simpler heat sources like the uniform heat generation rate are used [31]. Moreover, the interaction between the welding arc and workpiece while using the latest power sources is highly dynamic. The proposed numerical model demonstrates that the source term in heat transfer modelling is a trade-off between the physical phenomenon and the computations' complexity. The outcomes of the research presented here provide the significance of peak temperature for optimizing the heat source dimension, specifically for the AC square waveform submerged arc welding process and in general for other welding processes as well. The model can be further developed for predicting the relevant thermal and mechanical properties of the different geometric configurations of welds like T-Joint, lap joint, and groove welding.

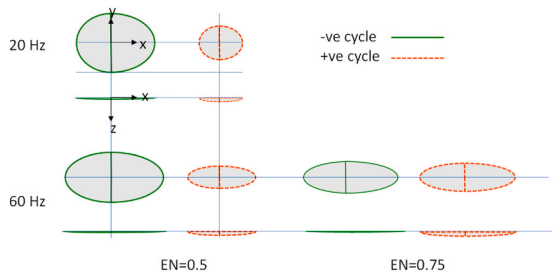

Fig. 10. Relation between process condition and heat source dimensions (relative dimension on same but not actual scale).

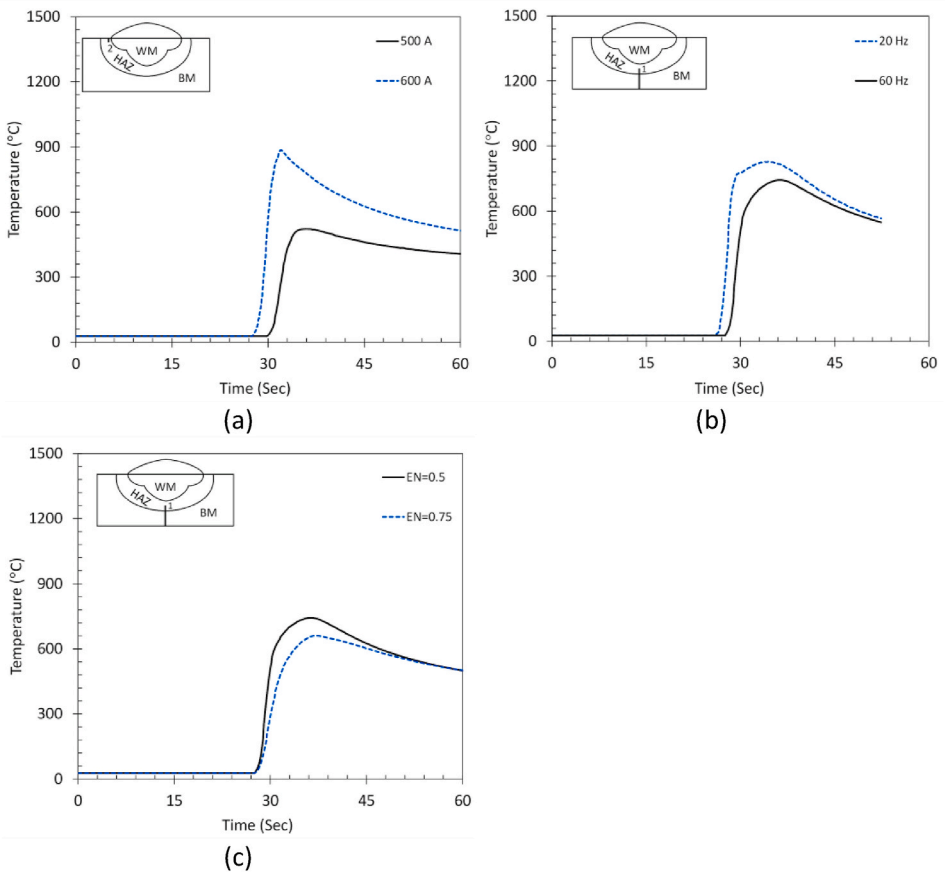

Fig. 11. Parametric effects on thermal cycle.

5. Conclusions

The article presents a new heat source model for the heat transfer analysis of the AC square wave welding process. The model is validated with the experiments. The influence of the welding process condition on the parameters of the heat source is explained. The following are the conclusions drawn from the current investigation:

1. The weld-pool's specific geometric features in the AC square waveform welding necessities a dedicated model to represent the heat source term in the heat transfer analysis. A scheme of two overlapping heat sources, representing the +ve and -ve cycles and those share the arc energy based on the electrode negativity ratio is presented.
2. The complexity arising out of the increased number of heat source parameters is dealt with a two-stage methodology. In the first stage, a steady-state heat source model is used to find the heat source dimension by inverse modelling the peak temperature. The heat source dimensions are then used for the transient thermal analysis to predict the thermal cycle and validate the developed model.

3. The heat source dimensions are strongly associated with the welding process conditions. The process parameters, such as welding current, current frequency and electrode negativity ratio, directly impacts the dimensions. The analysis of the interplay between the dimensions and the process parameters provides insight into the process; for example, the higher frequency stabilizes the arc on lowering the peak temperature.
4. Unlike the complex fluid dynamics-based model, the pure heat transfer analysis provides limited insight into the weld-pool happenings. However, the computationally affordable heat transfer models provide accurate thermal distribution in the workpiece's body. They thereby are useful to resolve shop-floor significant issues such as residual stress and distortion.

Credit Author Statement

Uttam Kumar: Investigation, Validation, Writing - Original Draft. Abhay Sharma: Conceptualization, Methodology, Software, Formal analysis, Writing - Review & Editing. Yohei Abe: Investigation. Takahiro Fujimoto: Investigation. Akikazu Kitagawa: Resources. Mitsuyoshi Nakatani: Resources. Manabu Tanka: Consultation. Testo Suga: Review, Project administration.

Declaration of competing interest

The authors declare that they have no known competing financial interests or personal relationships that could have appeared to influence the work reported in this paper.

Acknowledgement

The authors acknowledge the joint research agreement between KU Leuven and Joining and Welding Research Institute (JWRI), Osaka University, Japan, that facilitated this investigation's modelling and analysis phase. The experimental support provided under the joint project between Hitachi Zosen Corporation, Indian Institute of Technology Hyderabad, India, and JWRI, Osaka, Japan underGlobalizing Asian Networks Project (Ja19990018), is acknowledged.

References

[1] S. Choudhury, A. Sharma, U.K. Mohanty, R. Kasai, M. Komura, M. Tanaka, T. Suga, Mathematical model of complex weld penetration profile: a case of square AC waveform arc welding, J. Manuf. Process. 30 (2017) 483–491.
[2] U.K. Mohanty, A. Sharma, Y. Abe, T. Fujimoto, M. Nakatani, Kitagawa A. Kitagawa, M. Tanaka, T. Suga, Geometric model of the weld bead in DC and square AC submerged arc welding of 2.25 Cr-1 Mo heat resistant steel, in: Advances in Additive Manufacturing and Joining, Springer, Singapore, 2020, pp. 433–445.
[3] J. Goldak, A. Chakravarti, M. Bibby, A new finite element model for welding heat sources, Metall. Trans. B 15 (2) (1984) 299–305.
[4] Y. Li, Y.H. Feng, X.X. Zhang, C.S. Wu, An improved simulation of heat transfer and fluid flow in plasma arc welding with modified heat source model, Int. J. Therm. Sci. 64 (2013) 93–104.
[5] A. Sharma, N. Arora, S.R. Gupta, Investigation into arc behavior during twin-wire submerged arc welding, Mater. Manuf. Process. 25 (8) (2010) 873–879.
[6] G.X. Xu, C.S. Wu, G.L. Qin, X.Y. Wang, S.Y. Lin, Adaptive volumetric heat source models for laser beam and laser+ pulsed GMAW hybrid welding processes, Int. J. Adv. Manuf. Technol. 57 (1–4) (2011) 245–255.
[7] W. Piekarska, M. Kubiak, Three-dimensional model for numerical analysis of thermal phenomena in laser–arc hybrid welding process, Int. J. Heat Mass Tran. 54 (23–24) (2011) 4966–4974.
[8] S.S. Gajapathi, S.K. Mitra, P.F. Mendez, Part I: development of new heat source model applicable to micro electron beam welding, Sci. Technol. Weld. Join. 17 (6) (2012) 429–434.
[9] J. Chen, C.S. Wu, M.A. Chen, Improvement of welding heat source models for TIG-MIG hybrid welding process, J. Manuf. Process. 16 (4) (2014) 485–493.
[10] A.S. Azar, A heat source model for cold metal transfer (CMT) welding, J. Therm. Anal. Calorim. 122 (2) (2015) 741–746.
[11] A. Sharma, A.K. Chaudhary, N. Arora, B.K. Mishra, Estimation of heat source model parameters for twin-wire submerged arc welding, Int. J. Adv. Manuf. Technol. 45 (11–12) (2009) 1096.
[12] A.S. Azar, S.K. Ås, O.M. Akselsen, Determination of welding heat source parameters from actual bead shape, Comput. Mater. Sci. 54 (2012) 176–182.
[13] X. Jia, J. Xu, Z. Liu, S. Huang, Y. Fan, Z. Sun, A new method to estimate heat source parameters in gas metal arc welding simulation process, Fusion Eng. Des. 89 (1) (2014) 40–48.
[14] N. Yadaiah, S. Bag, Development of egg-configuration heat source model in numerical simulation of autogenous fusion welding process, Int. J. Therm. Sci. 86 (2014) 125–138.
[15] T.F. Flint, J.A. Francis, M.C. Smith, J. Balakrishnan, Extension of the double-ellipsoidal heat source model to narrow-groove and keyhole weld configurations, J. Mater. Process. Technol. 246 (2017) 123–135.
[16] A. Ghosh, A. Yadav, A. Kumar, Modelling and experimental validation of moving tilted volumetric heat source in gas metal arc welding process, J. Mater. Process. Technol. 239 (2017) 52–65.
[17] J.P. Faria, H.D. Miranda, M.F. Motta, F.D.Q. Paiva, E.F. Pessoa, Effect of square-wave AC GMAW on weld beam geometry, Weld. Int. 21 (3) (2007) 212–219.
[18] R.E. Toma, S.D. Brandi, A.C. Souza, Z. Morais, Comparison between DC (+) and square wave AC SAW current outputs to weld AISI 304 for low-temperature applications, Weld. J. 90 (9) (2011) 153S–160S.
[19] U.K. Mohanty, A. Sharma, M. Nakatani, A. Kitagawa, M. Tanaka, T. Suga, A semi-analytical nonlinear regression approach for weld profile prediction: a case of alternating current square waveform submerged arc welding of heat resistant steel, J. Manuf. Sci. Eng. 140 (11) (2018), 111013(1-11).
[20] Y. Wang, M. Chen, C. Wu, High-frequency pulse-modulated square wave AC TIG welding of AA6061-T6 aluminum alloy, Weld. World (2020) 1–14.
[21] K. He, Z. Zhou, C. Wang, X. Li, Arc signal analysis of square wave alternating current submerged arc welding using local mean decomposition, J. Adv. Mech. Des. Syst. Manuf. 10 (9) (2016). JAMDSM0104-JAMDSM0104.
[22] U.K. Mohanty, Y. Abe, T. Fujimoto, M. Nakatani, A. Kitagawa, M. Tanaka, T. Suga, A. Sharma, Performance evaluation of alternating current square waveform submerged arc welding as a candidate for fabrication of thick welds in 2.25 Cr-1Mo heat-resistant steel, J. Pressure Vessel Technol. 142 (4) (2020), 041506 (1-11).
[23] A. Sharma, N. Arora, B.K. Mishra, A practical approach towards mathematical modeling of deposition rate during twin-wire submerged arc welding, Int. J. Adv. Manuf. Technol. 36 (5–6) (2008) 463–474.
[24] E. Nart, Y. Celik, A practical approach for simulating submerged arc welding process using FE method, J. Constr. Steel Res. 84 (2013) 62–71.
[25] H.H. Zargari, K. Ito, M. Kumar, A. Sharma, Visualizing the vibration effect on the tandem-pulsed gas metal arc welding in the presence of surface tension active elements, Int. J. Heat Mass Tran. 161 (2020) 120310.

[26] S.Q. Moinuddin, A. Kapil, K. Kohama, A. Sharma, K. Ito, M. Tanaka, On process–structure–property interconnection in anti-phase synchronized twin-wire GMAW of low carbon steel, Sci. Technol. Weld. Join. 21 (6) (2016) 452–459.
[27] A. Sharma, N. Arora, B.K. Mishra, Mathematical modeling of flux consumption during twin-wire welding, Int. J. Adv. Manuf. Technol. 38 (11–12) (2008) 1114–1124.
[28] K. He, Q. Li, J. Chen, An arc stability evaluation approach for SW AC SAW based on Lyapunov exponent of welding current, Measurement 46 (1) (2013) 272–278.
[29] C.O.N.G. Baoqiang, Q.I. Bojin, Influence of current converting speed on 2219 aluminum alloy VPTIG weld joints, Trans. China Weld. Inst. 8 (2010).
[30] M. Kumar, S.Q. Moinuddin, S.S. Kumar, A. Sharma, Discrete wavelet analysis of mutually interfering co-existing welding signals in twin-wire robotic welding, J. Manuf. Process. (2020). https://doi.org/10.1016/j.jmapro.2020.04.048.
[31] S. Reddy, M. Kumar, J.S. Panchagnula, P.K. Parchuri, S.S. Kumar, K. Ito, A. Sharma, A new approach for attaining uniform properties in build direction in additive manufactured components through coupled thermal-hardness model, J. Manuf. Process. 40 (2019) 46–58.